

UC Irvine

UC Irvine Previously Published Works

Title

Automated detection of brain abnormalities in neonatal hypoxia ischemic injury from MR images.

Permalink

<https://escholarship.org/uc/item/13s3b4vz>

Journal

Medical image analysis, 18(7)

ISSN

1361-8415

Authors

Ghosh, Nirmalya
Sun, Yu
Bhanu, Bir
et al.

Publication Date

2014-10-01

DOI

10.1016/j.media.2014.05.002

Peer reviewed



Automated detection of brain abnormalities in neonatal hypoxia ischemic injury from MR images



Nirmalya Ghosh^{a,1}, Yu Sun^{b,1}, Bir Bhanu^b, Stephen Ashwal^a, Andre Obenaus^{a,c,*}

^a Department of Pediatrics, Loma Linda University, School of Medicine, Loma Linda, CA 92354, USA

^b Center for Research in Intelligent Systems (CRIS), University of California, Riverside, CA 92521, USA

^c Cell, Molecular and Developmental Biology Program and Department of Neuroscience, University of California, 1140 Bachelor Hall, Riverside, CA 92521, USA

ARTICLE INFO

Article history:

Received 5 October 2013

Received in revised form 23 April 2014

Accepted 10 May 2014

Available online 16 May 2014

Keywords:

Hypoxia ischemic injury

Hierarchical region splitting

Watershed

Symmetry

Arterial ischemic stroke

ABSTRACT

We compared the efficacy of three automated brain injury detection methods, namely symmetry-integrated region growing (SIRG), hierarchical region splitting (HRS) and modified watershed segmentation (MWS) in human and animal magnetic resonance imaging (MRI) datasets for the detection of hypoxic ischemic injuries (HIIs). Diffusion weighted imaging (DWI, 1.5T) data from neonatal arterial ischemic stroke (AIS) patients, as well as T2-weighted imaging (T2WI, 11.7T, 4.7T) at seven different time-points (1, 4, 7, 10, 17, 24 and 31 days post HII) in rat-pup model of hypoxic ischemic injury were used to assess the temporal efficacy of our computational approaches. Sensitivity, specificity, and similarity were used as performance metrics based on manual ('gold standard') injury detection to quantify comparisons. When compared to the manual gold standard, automated injury location results from SIRG performed the best in 62% of the data, while 29% for HRS and 9% for MWS. Injury severity detection revealed that SIRG performed the best in 67% cases while 33% for HRS. Prior information is required by HRS and MWS, but not by SIRG. However, SIRG is sensitive to parameter-tuning, while HRS and MWS are not. Among these methods, SIRG performs the best in detecting lesion volumes; HRS is the most robust, while MWS lags behind in both respects.

© 2014 Elsevier B.V. All rights reserved.

1. Introduction

Magnetic resonance imaging (MRI) datasets contain information that characterize normal and abnormal tissues based on their MR physical properties and anatomical locations. In clinical trials, MRI indices are used as outcome measures to assess pathological changes and to monitor treatment efficacy (Schiemanck et al., 2006). Traditionally, regions or boundaries of interest (ROI) on MRI, either in healthy or injured tissues are manually traced and can be fraught with inconsistencies between users, potential biases, difficulty in replicating data, and low throughput (Niimi et al., 2007). Computational advances in efficient ROI detection algorithms are important for (1) clinical diagnosis, (2) assessment of treatment and (3) experimental and clinical research objectives (Ghosh et al., 2012a).

Advances in computer vision and pattern recognition have made inroads using several computational ROI detection techniques in medical MRI data (Anbeek et al., 2008; Bergo et al., 2008; Birgani et al., 2008; Cuadra et al., 2004; Hojjatoleslami and Kruggel, 2001; Kabir et al., 2007; Kharrat et al., 2009; Khotanlou et al., 2009; Manana et al., 2006; Ray et al., 2007; Saha and Bandyopadhyay, 2007; Van Leemput et al., 2001; Zhiguo et al., 2005). Comparison of these existing methods (Table 1) reveals several computational challenges, including: (a) partial volume effects, (b) low contrast, and (c) motion artifacts that blur ROI/anatomical boundaries (Table 2). These challenges still remain even after a range of proposed solutions to improve computational assessments, including registration (Schmidt et al., 2005), normalization (Kabir et al., 2007), or use of prior brain tissue models particularly for adult MR data (Birgani et al., 2008). While prior probabilistic models for brain anatomy and specific diseases have been used (Corso et al., 2008), they are not robust to injury induced brain distortions, as model-subject co-registration often fails (Cuadra et al., 2004; Ghosh et al., 2012a). Curve fitting based methods like active contour snakes (Droske et al., 2001; Liang et al., 2006; Zhou and Xie, 2013), level-set propagation (Droske et al., 2001) and their combined and/or modified versions (Bai

* Corresponding author. Address: Department of Pediatrics, Loma Linda University, 11175 Campus Street, Rm A1120, Loma Linda, CA 92354, USA. Tel.: +1 909 558 7108; fax: +1 909 558 7519.

E-mail address: aobenaus@llu.edu (A. Obenaus).

¹ Both authors contributed equally to this work.

Table 1

Overview of state-of-the-art MRI based injury detection methods. Last three rows (in gray) summarize the methods we used in our comparisons.

Author	Methods		Automation			Comments
	Segmentation	Injury detection	Alignment	Prior model	Training	
Birgani et al. (2008)	Fuzzy Cluster Neural Network	Model-based detection	NO	YES	NO	Need to set the number of classes; need ROI prior model.
Kabir et al. (2007)	Maximum <i>a posteriori</i> (MAP)	Multimodal Markov random field (MRF)	YES	YES	YES	Need to know the distribution of lesion intensities.
Khotanlou et al. (2009)	Expectation Maximization (EM) with MRF	EM	NO	YES	NO	The prior model contains only limited categories of brain tissues.
Cuadra et al. (2004)	Adaptive statistical algorithm	Model of lesion growth	YES	YES	NO	Too many model dependent steps; less robust.
Anbeek et al. (2008)	Manually by experts	<i>K</i> -Nearest neighbors	NO	YES	YES	The detected lesion contains too many noisy regions.
Hojjatoleslami and Kruggel (2001)	Region growing	Manual Lesion location	NO	NO	NO	The lesion needs to be located manually.
Corso et al. (2008)	Weighted aggregation	Gaussian Mixture Model (GMM)	NO	YES	YES	Lesions contain too many noisy regions.
Kruggel et al. (2008)	Texture-based segmentation	Gaussian –based clustering	YES	YES	NO	Lesions contain too many noisy regions.
Nan et al. (2009)	Region growing	Multi-kernel based SVM	NO	YES	NO	Support vector machine (SVM) is insufficient in lesion clustering.
Liu et al. (2005)	Fuzzy connectedness segmentation	Fuzzy volume rendering	YES	YES	NO	User needs to locate tumor regions manually.
Schmidt et al. (2005)	Soft-margin SVM	Model-based detection	YES	YES	NO	Performance depends on the complex alignment step.
Kharrat et al. (2009)	Wavelet-based segmentation	<i>K</i> -means clustering	NO	YES	NO	High fuzziness on detected boundaries.
Sun and Bhanu (2012)	Symmetry-based region growing	EM classifier	NO	NO	NO	MRI-specific parameters; high level features.
Ghosh et al. (2011)	Hierarchical region splitting	Area-based detection	NO	YES	NO	ROIs in many sub-images; possible over-segmentation; low level features.
Ratan et al. (2009)	Watershed boundaries followed by similarity based merging	Manual allocation	NO	YES	NO	Over-segmentation occurs; requires manual derived prior knowledge; low level features.

Table 2

Challenging problems in injury detection from MRI data and how three methods overcome these challenges.

Problems		Methods which overcome these challenges		
ID	Details	Symmetry Sun and Bhanu (2012)	HRS Ghosh et al. (2011)	Watershed Ratan et al. (2009)
(1)	Insufficient cues/features to discriminate between ROI and normal tissues. Only low-level cues (features), e.g., gray scale, texture or shape, are used to extract the ROIs, leading to a low detection accuracy.	Uses symmetry as a new cue, which is able to discriminate between ROIs and normal tissues. It is automatic and without prior models.	Use prior knowledge (mean MR values of sub-regions) to detect ROI.	Manual initialization for prior knowledge (position and mean gray scale values of the ROIs).
(2)	Blurred boundaries between tissues belonging to different tissue structures. These are partially caused by the loss of resolution and contrast during the collection and digitization of a MR image, mainly due to partial volume effects.	The blurred boundary is outlined properly.	Segment regions at different levels.	Outlines small and blurred region boundaries.
(3)	Movement artifacts due to the subjects's head movement during scanning that result in recording errors, especially for MR sequences taken at different time points. Different MRI slices might have different motion artifacts and hence different noise levels that present an additional challenge for image pre-processing due to image-dependent variations in image contrast.	No registration or alignment is needed. It is invariant to rotation and scaling.	Same as symmetry method.	Same as symmetry method.

et al., 2013; Kazemifar et al., 2014; Le Guyader and Vese, 2008; Liang et al., 2006; Mesejo et al., 2014; Somkantha et al., 2011; Wang et al., 2013) have been applied to medical image segmentation. However, these methods suffer from manual interventions (Liang et al., 2006; Zhou and Xie, 2013), computational complexity (Kazemifar et al., 2014; Mesejo et al., 2014), dependence on MRI contrast levels (Kazerooni et al., 2011; Liang et al., 2006; Somkantha et al., 2011) and inadequate cues for efficient registration to prior-models (Bai et al., 2013; Le Guyader and Vese, 2008; Wang et al., 2013) and atlases (Kazemifar et al., 2014), specifically in low-contrast noisy MRI data (Zhou and Xie, 2013).

Moreover, for neonatal brains, age-matched brain maps and prior models are not readily available (due to scarce data from healthy controls) and often cannot be co-registered easily as a result of increased water content and structural variability in immature brains (Ghosh et al., 2012a). Thus, MRI based automated detection of neonatal brain injury remains extremely challenging and a comparative study of different techniques might bring forth case-specific applications and future computational improvements by wisely fusing more than one technique.

The rationale for undertaking the current study was two-fold: firstly, to compare three fully automated computational

approaches to study neonatal HII without using any prior models or brain atlases, and secondly to evaluate these methods for serial MRI data, as the ischemic lesion rapidly evolves. We tested all aspects first in our well characterized model of rodent neonatal HII followed by validation using human HII MRI data. We report on the comparative usage of three state-of-the-art computational methods for ROI detection from MR images following neonatal HII. Specifically, we assessed a symmetry-integrated region growing (SIRG) method (Sun and Bhanu, 2009; Sun et al., 2009), a hierarchical region splitting (HRS) method (Ghosh et al., 2011), and a modified watershed (MWS) method (Ratan et al., 2009). Using MRI data from an animal model and patients with neonatal ischemia, the performance of these three methods were compared to manually detected ground-truths based on usage of prior knowledge, volumetric accuracy, regional overlap and robustness (lesion detection in multiple MR slices and across cohorts). We found that for evolving neonatal ischemic injury, SIRG performed best overall but HRS was the most robust, and fusion of these two techniques in future studies has a greater potential for automated injury detection from brain MRI data.

2. Materials and methods

2.1. Clinical and animal MRI data

All three of our computational methods were tested on animal and human datasets. In our animal studies we utilized postnatal 10 days old rat pups that underwent neonatal HII, using the Rice–Vannucci Model (RVM) of unilateral permanent carotid artery ligation with 8% hypoxia (Ghosh et al., 2012a). The current study utilized neonatal rats ($n = 4$) at seven different time points to monitor the evolution of ischemic injury. In addition, $n = 4$ rodents were also assessed at a lower MR field strength (4.7T) at later time-points. T2-weighted images (T2WI) were acquired at seven different time-points (1, 4, 7, 10, 17, 24 and 31 days) post induction of HII. This range of time points was chosen based on previous studies that revealed the dynamic nature of the evolving HII injury (Obenaus et al., 2011a). All animal protocols were approved by the Loma Linda University (LLU) Institutional Animal Care and Use Committee. Key imaging acquisition parameters are summarized in Table 3 (see also (Ghosh et al., 2011)).

In our clinical data sets we utilized diffusion weighted imaging (DWI) and their quantitative apparent diffusion coefficient (ADC) maps from neonatal patients ($n = 2$) evaluated for arterial ischemic stroke (AIS). De-identified neonatal data were acquired at 3–5 days post injury (Ghosh et al., 2012b). Use of all patient data were approved by LLU Institutional Review Board (see Table 3).

Table 3
Neuroimaging acquisition parameters for rodent and human MRI.

Parameters	11.7T (rodent) T2	4.7T (rodent) T2	1.5T (human) DWI
Repetition time (ms)	2358	3563	3000
Echo time (ms)	10.21	20	110
Echoes/ b -values (s/mm^2)	10	6	0, 1000
Number of averages	4	2	1
Field of view (cm)	2×2	3×3	220×220 – 240×240
Matrix	128×128	128×128	256×256
Number of slices	20	25	17
Slice thickness (mm)	0.5–1	1	4–5
Inter-slice gap (mm)	1	1	1.2–1.5
Acquisition time (min)	20	12	1.5–3.8

In both experimental animal models and human MR data, experienced evaluators provided ground-truth manually derived ROIs for comparison and testing purposes. As we found earlier that inter-observer variability for lesion detection is small (Ghosh et al., 2012b), we have used the mean ROI location from two experienced raters as the gold-standard for comparison. A minor caveat is that both SIRG and MWS methods used relative intensity based TIFF images whereas HRS can directly utilize T2-relaxation and ADC values for detection. In addition, skull stripping and brain extraction from MRI data was performed by HRS using published preprocessing steps (Ghosh et al., 2012b).

2.2. Lesion detection by symmetry-integrated region growing (SIRG)

The SIRG lesion detection method (Sun and Bhanu 2009; Sun et al., 2009) takes the original MR image (Fig. 1a), finds the axis of symmetry (Fig. 1b), derives a symmetry affinity matrix (Fig. 1c) that is used as a measure of symmetry in later steps. The next step enhances segmentation results by verifying that the symmetric parts are segmented appropriately (Fig. 1d), followed by computation of kurtosis and skewness from the symmetry affinity matrix which are used to extract the asymmetric regions from segmented brain (Fig. 1e). Simultaneously, the symmetry affinity matrix (Fig. 1c) from each MRI slice is also used for clustering and identification of asymmetric groups using 3D relaxation techniques (Fig. 1f). The 3D relaxation and kurtosis/skewness results are then fused to obtain a more refined asymmetric region (Fig. 1g). Finally, an unsupervised classifier extracts the regions of injury from the asymmetric regions (Fig. 1h) by incorporating 3D information from 2D MRI slices as an additional new feature (Fig. 1, right panel). Key parameters used in SIRG method are summarized in Table 4.

Symmetry Extraction: A high-speed method was used to extract the global reflective symmetry axis of the brain. We used a *global symmetric constellation of features* (Lowe, 2004) to detect the symmetry axis of the MRI brain images (Fig. 1b), that were then utilized to compute a symmetry affinity matrix (Fig. 1c), which is a cross-correlation between the original image and the symmetrically reflected image. The value of each point in an affinity matrix corresponds to the pixel's symmetry level, valued from 0 (symmetric) to 1 (asymmetric). The symmetry affinity measure is computed using the Curvature of Gradient Vector Flow (CGVF) method (Gupta et al., 2005; Prasad and Yegnanarayana, 2004).

Segmentation: We utilized a symmetry-integrated region growing segmentation approach (Sun and Bhanu, 2009; Sun et al., 2009; Sun and Bhanu, 2012) to segment the brain into different tissues. The pixels i and neighboring region j with similarity less than a threshold $\delta(i, j) < \delta_g$ is grown into a larger region. The similarity $\delta(i, j) = \delta_R(i, j)\delta_S(i, j)$ is composed of the region feature similarity and the symmetry similarity constraints, respectively. Traditional region growing segmentation accepts color, gray scale, texture or shape as a similarity constraint $\delta_R(i, j)$ for segmentation (Nan et al., 2009). However, we included a symmetry constraint derived from the symmetry affinity matrix which was integrated into the region growing algorithm as shown below:

$$\delta_S(i, j) = \frac{\frac{\pi}{2} + \text{actan}(\sqrt{(1+C_i)(1+C_j)})}{\pi} + \frac{1 + |\sqrt{C_i} - \sqrt{C_j}|}{2} \quad (1)$$

where C_i and C_j are symmetry affinities of pixel i and neighboring region j . For the first term of Eq. (1), if both patterns i and j indicate low symmetry affinities (highly symmetric), they are more likely to be aggregated by decreasing the constraint $\delta_S(i, j)$; while the second term favors more similar symmetry affinities. This results in tissues being segmented more symmetrically (see Fig. 1d).

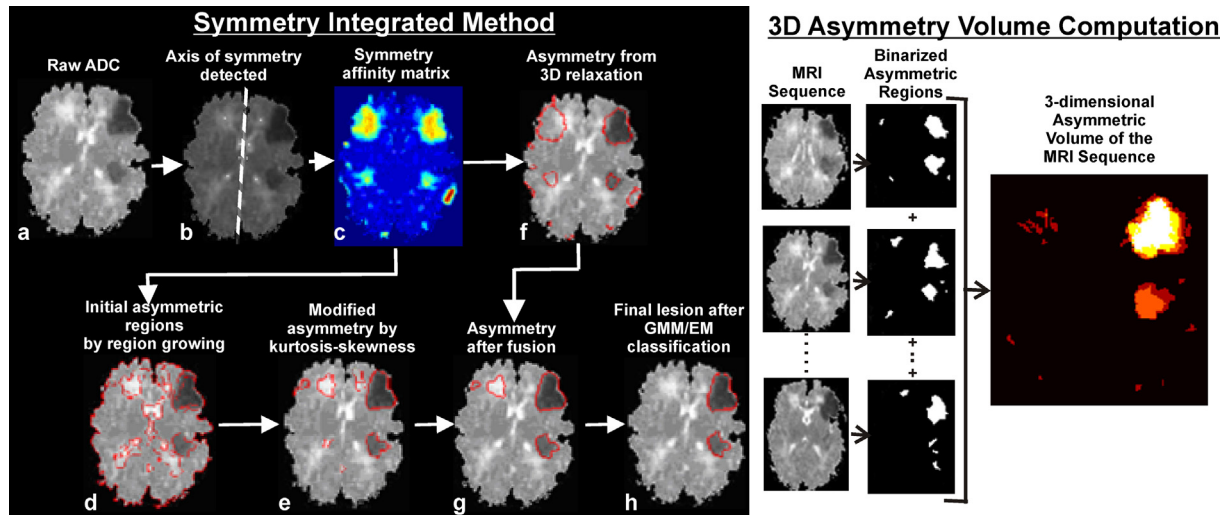


Fig. 1. Symmetry integrated region growing (SIRG) based lesion detection (Left Panel). SIRG lesion detection in a newborn AIS data starts with the original ADC map (a) from which the axis of symmetry (AoS) was detected (dotted line) (b). A symmetry affinity matrix was computed where brighter (yellow) regions are more asymmetric across the AoS (c). The SIRG algorithm then extracted these initial asymmetric regions (d) which were then modified using kurtosis-skewness measures of the regions (e). A separate algorithm identified asymmetric clusters using a 3D gradient relaxation algorithm (f). Robust asymmetric regions from (e) and (f) were then fused (g), from which, GMM/EM then classified the stroke (AIS) regions (h). 3D asymmetry volume computation (Right Panel). Binary masks of the ischemic lesion were detected in 2D and then each slice was added to sum the lesion from the entire brain. 3D connectivity was color coded to visualize relative reliability of 2D detections to the final 3D asymmetry ischemic injury volume. (For interpretation of the references to colour in this figure legend, the reader is referred to the web version of this article.)

Table 4

Parameter sets for injury detection utilized for our comparative three methods.

Authors	Parameters (thresholds)
Symmetry Sun and Bhanu (2012)	<ol style="list-style-type: none"> Region growing segmentation: <ol style="list-style-type: none"> pixel aggregation criterion; region merging criterion; Asymmetric region extraction: <ol style="list-style-type: none"> region's mean kurtosis and skewness of symmetry affinity values; region's mean symmetry affinity value; number of iterations in 3D relaxation; percentage of overlap for final asymmetric region extraction. very small segments are filtered before ROI detection.
HRS Ghosh et al. (2011)	<ol style="list-style-type: none"> Region split stopping criteria: <ol style="list-style-type: none"> area of the region; standard deviation of region's MR values; kurtosis of region's MR values; ROI detection: <ol style="list-style-type: none"> region's approximate mean MR values.
Watershed Ratan et al. (2009)	<ol style="list-style-type: none"> Watershed segmentation: <ol style="list-style-type: none"> region merging criterion; ROI detection (manually): <ol style="list-style-type: none"> position of ROI; region's mean MR values.

Asymmetric Region Extraction: Symmetry-based segmentation separated the segmented regions as either symmetric or asymmetric, in which the asymmetric regions contained the ROI. The final asymmetric regions (Fig. 1g) were a fusion of the results from the asymmetric regions by region growing (Fig. 1d) followed by region kurtosis/skewness asymmetry determinations (Fig. 1e) and the segmentation of the symmetry affinity matrix (Fig. 1f). The asymmetric segments (Fig. 1e) were extracted from all segmented regions based on kurtosis and skewness of the symmetry affinity matrix (Sun et al., 2009). Larger kurtosis of a region's symmetry affinity values indicated more deviation in the region's

symmetry affinity distribution (Du and Kopriva, 2008), which was designated as an asymmetric region. The negative skewness of a region means that its symmetry affinity distribution is left-tailed, which also indicates an asymmetric region. Separately, 3D asymmetry was extracted (Fig. 1f) using a 3D relaxation method (Bhanu and Parvin, 1987). This algorithm segmented the symmetry affinity matrix by iteratively separating its histogram into two classes, symmetric and asymmetric. The final step was to determine the asymmetric regions by identifying at least 50% overlap between the asymmetry from 3D relaxation (Fig. 1f) and kurtosis/skewness steps (Fig. 1e).

ROI Extraction: The derived asymmetric regions were potential candidates for designation as putative HII lesions. An unsupervised Expectation Maximization (EM) classifier with Gaussian Mixture Model (GMM) (Bilmes, 1998) was used to classify candidate asymmetric regions (see Fig. 1g) into two classes: lesion vs. non-lesion using a 2D feature composed of region's gray scale intensity and the 3D asymmetry volumes assembled from the 2D slices (Fig. 1, right panel). Mean intensity values of normal and injured tissues were first estimated from a small training set comprised of three MRI slices from each dataset, and the classifier was then trained by unsupervised EM around those mean values as the centers of GMM. The 3D asymmetry volume then became the 3D binary mask for the final asymmetric regions. The binary results of all slices from the MRI dataset were summed together to build a 3D asymmetry volume image (Fig. 1, right panel), where groups of brighter pixels in the 2D asymmetry volume image indicate larger asymmetric volume values, in which the lesion was located. The mean 3D asymmetry volume of each asymmetric region (Fig. 1g) was used as a feature for classification, where increased mean 3D asymmetry volumes were identified as the ROI (lesion) class (Fig. 1h). The classification by EM/GMM using these features is unsupervised and fully automated.

2.3. Lesion detection by hierarchical region splitting (HRS)

HRS is an automated and recursive region segmentation method that segments MR images based on either image intensities or on quantitative MR values (T2 relaxation times, ADC values),

into uniform image regions recursively. In each recursive splitting, regions from the previous step (iteration) were separated into smaller yet more uniform image regions (Ghosh et al., 2011). The brain exhibits different contrast levels between anatomically distinct brain tissues (e.g., cortex vs. striatum) and thus, a uniform region within the brain likely represents a single brain tissue type. MRI contrast levels within the brain can be further altered by disease, such as HII, where increased T2 relaxation values (or increased image intensities) reflect increased water content indicative of edema. Similar increases/decreases in ADC occur in HII. The HRS method exploited these differences to segment uniform regions in which brighter signal on T2 maps was expected to indicate the location of the brain lesion. Similarly, ADC maps reflect water mobility and as many lesions have restricted water mobility compared to normal brain tissues at the early stage of the injury (Ghosh et al., 2012a), the HII lesions are hypo-intense (darker) in ADC maps so that HRS can separate these regions during recursive splitting (Fig. 2).

The HRS sequence was comprised of: **Rescaling**: To reduce computational complexity and increase robustness to MRI signal variation, we rescaled the T2WI or ADC values to a range [0, 255] and the scaling factors were saved to map the automatically derived results in image intensity values back to the original MR (T2 or ADC) values. As T2 values >255 ms are not typical, rescaled data are very similar to the actual T2 values. For ADC maps (or other MRI modalities), this rescaling step made HRS generic and compatible to any range of MR values. **Deriving the HRS histogram**: The signal spectrum histogram $H(i)$ of the rescaled MRI was computed, where $i = [1, 2, \dots, N = 255]$. **Computing adaptive segmentation threshold**: Similar to Otsu's method (Otsu, 1979), we modeled the MRI histogram at every region splitting level (i.e., level 0–2 in Fig. 2B) as a bimodal distribution with two distinct and distant peaks (see Fig. 2A). Histogram H was normalized to estimate the probabilistic distribution function, $p(i) = H(i) / \sum_{i=1}^N H(i)$, and the cumulative distribution function $\Omega(i) = \sum_{j=1}^i p(j)$. The cumulative weighted means at every intensity value $u(i) = \sum_{j=1}^i p(j) \cdot j$ and the final cumulative mean $\mu_t = \mu(N)$ were used to compute the sequence of Otsu's measure,

$$\delta_b^2(i) = \frac{[\mu_t \cdot \Omega(i) - \mu(i)]^2}{\Omega(i) \cdot (1 - \Omega(i))} \quad (2)$$

where its mode(s) defined the valley of the original distribution $p(i)$. For more than one closely-spaced modes, we used the mean $idx = \text{mean}[\text{modes}(\sigma_b^2)]$ as the valley and computed the threshold (valley of $p(i)$) by $Th = (idx - 1)$. Threshold Th defined the valley between these peaks as an adaptive threshold to split the image into two sub-region images (Fig. 2A), in which one region has values greater and the other region has values less than the threshold Th . Each peak was a region with a minimum intra-regional and maximum inter-regional MR variance. **Recursive bimodal segmentation**: A unique aspect of the HRS method was its recursive application of the above bi-partite segmentation. The sub-images were then recursively further split to generate a tree-like hierarchical data structure (Fig. 2B) which we describe as the HRS tree. **Criteria for stopping segmentation**: Recursive splitting was continued until individual segments or sub-regions have near-uniform MRI intensities. Uniformity was measured based on three factors, whether: (a) the individual connected regions were small (area < 50 pixels = 2 ml in neonatal rat brain) and unlikely to be from different tissue-types; (b) the MR signal value for the region had a low standard deviation (STD < 10 rescaled MR values), that is, the regional MRI intensities were relatively uniform; and (c) the MR histogram for the segmented region had a low kurtosis value (kurtosis < 1.5) where the peak was too distinct to be modeled as a bimodal distribution. The brain regions obtained from HRS (e.g., HRS trees in Fig. 2B) were not always uniform in MR (or rescaled MR) values, but as we descended down the HRS tree, we achieved greater uniformity within individual regions. The threshold values or split-stopping criteria (area < 50; STD < 10; kurtosis < 1.5) were selected based on published results (Ghosh et al., 2011). These thresholds did not affect ROI detection but minimized unnecessary over-segmentation of small or very uniform regions and thus, reduced HRS tree size and computational (space and time) complexity. **Scale-back to actual MR values**: The statistics (e.g., mean, standard deviation) of each HRS sub-regions were rescaled back to actual MR values using the saved scaling-factors (see above). **Detection of Lesion**: Based on previously published studies and established T2 and ADC ranges of normal brain tissues (Ghosh et al., 2011; Ghosh et al., 2012a), we used a T2 relaxation time of 75 ms (in animal data) and ADC value of $100 \times 10^{-5} \text{ mm}^2/\text{sec}$ (for clinical data) that could efficiently delineate the HII lesion from normal tissues. The method used these values as a soft threshold for the lesion mean, called *meanTh*. It

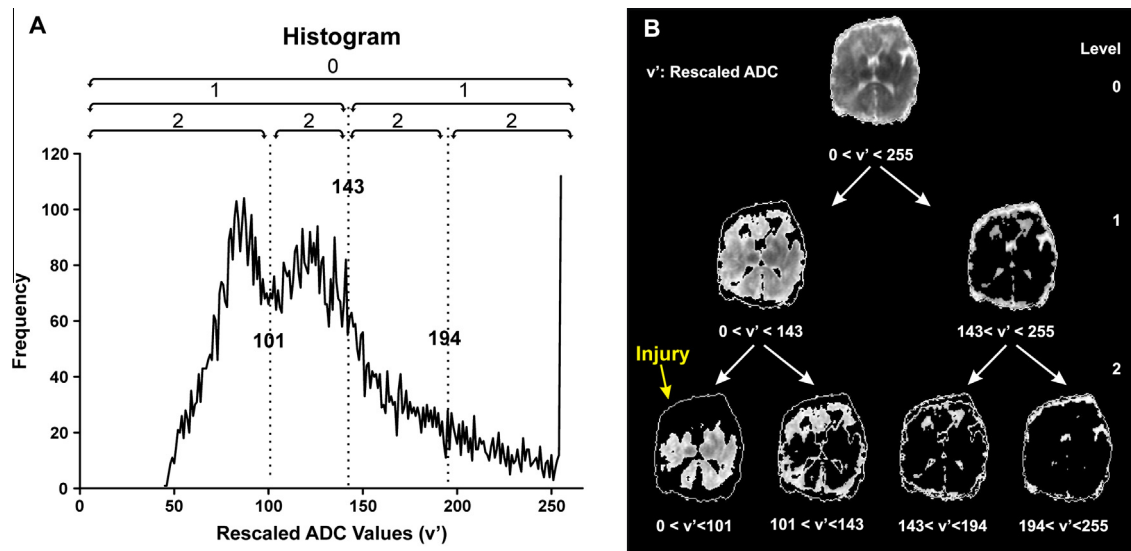


Fig. 2. Hierarchical region splitting (HRS) based lesion extraction. (A) ADC histogram: ADC values were rescaled (v') to an intensity range [0–255]. The HRS method then fitted a bimodal distribution and detected a valley (at $v' = 143$ in this example) as the threshold to split the histogram. This splitting was repeated recursively (next level thresholds were $v' = 101$ and 194). (B) HRS tree: Segmenting the ADC map into regions with v' values derived from the histogram formed the HRS tree. HRS automatically detected the left image in Level 2 as the ischemic lesion (arrow – injury). Only part of the complete HRS tree is shown.

accomplished this by systematically checking the (mean \pm standard deviation) value of the sub-regions in the HRS tree one by one, starting from the top (level 0) and gradually descending down branches of the HRS tree until reaching a sub-region with: (a) either (mean – standard deviation) was greater than the *meanTh* (=75) for T2-based HRS trees, (b) or (mean + standard deviation) was less than the *meanTh* (=100) for ADC-based HRS trees. HRS then categorized this sub-region as an ischemic lesion (Fig. 2B). The threshold – *meanTh* was the cutoff for the MR mean of HII lesion. Use of regional standard deviations (unlike those reported (Ghosh et al., 2011)) improved outlier rejection. Key HRS parameters are summarized in Table 4. Finally, regional properties (area, mean, and standard deviation), and 3D volumes of the injury were computed.

2.4. Lesion detection by modified watershed segmentation (MWS)

The watershed algorithm has been used for brain tumor segmentation and has been validated for segmentation and lesion detection from MRI datasets (Ratan et al., 2009). This method can segment ROIs provided that the desired parameters for segmentation and ROI properties are properly set. A conceptually simple supervised image-based (shape, texture, and content) technique was utilized here to analyze MRI brain images with relatively low computational requirements. The process flow of this methodology is shown in Fig. 3A. First, the following ‘multi-parameter’ features of the brain images were extracted: the image contrast edges (E), gray values (G), and local contrast (H). Then, the watershed segmentation method separated the brain into different compartments. Finally, injury regions were detected from the segmented regions by a supervised classifier. Key MWS parameters are summarized in Table 4.

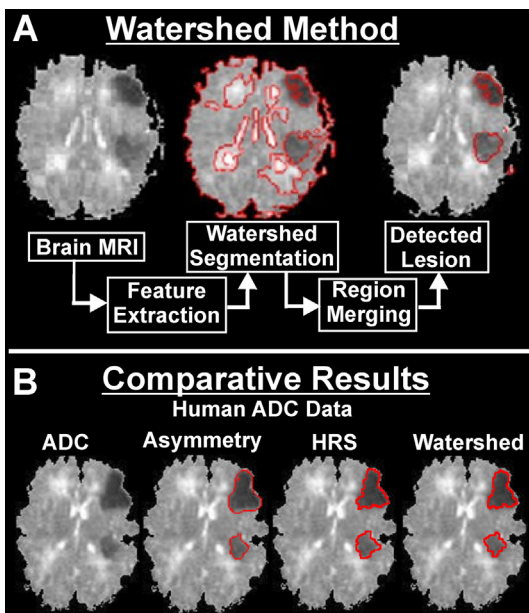


Fig. 3. (A) modified watershed segmentation (MWS) based lesion detection. Multi-parameter image feature – grayscale intensities, Sobel contrast edges, and local contrast indices were evaluated. These features formed a topological map where MWS started from regional peaks, followed droplet paths defined by a Genetic Algorithm, and reached the catchment basins that marked segmentation boundaries. To counter over-segmentation that is often encountered in watershed segmentation, similarity based region merging was performed. Finally, prior knowledge from testing data and ground-truth results were utilized to classify the segmented regions into either lesion, normal brain or outlier regions. (B) Comparative results for human ADC data. Representative results for a single ADC map image from an AIS patient illustrated that SIRG, HRS and MWS methods extracted comparable lesion regions.

Multi-parameter Calculation: The image contrast edge (E) parameter is often used to determine the boundaries of an object, based on the assumption that semantically similar objects have closer edges. Given this understanding, we used the Sobel edge detection method to detect image edges (I_E), obtained by filtering an input image with two convolution kernels (Sobel Kernels) concomitantly, to detect changes in vertical and horizontal contrasts, as I_x and I_y respectively. Image output (I_E) was obtained by calculating the gradient magnitude of each pixel (x_p, y_p) of the filtered images I_x and I_y , as shown in Eq. (3). Subsequently, the edge parameter (E) of a pixel (x_p, y_p) was calculated, whereby E was increased by one each time when $I_E(x_{p-n}, y_{p-n}) = '1'$ (indicating as an edge pixel), as shown in Eq. (4), where (x_{p-n}, y_{p-n}) was any neighboring pixel in an m by m block B centered at the pixel (x_p, y_p).

$$I_E(x_p, y_p) = \sqrt{I_x^2(x_p, y_p) + I_y^2(x_p, y_p)} \quad (3)$$

$$E(x_p, y_p) = \sum_{(x_{p-n}, y_{p-n}) \in B} (I_E(x_{p-n}, y_{p-n}) = 1) \quad (4)$$

The gray values (G) parameter was the gray scale value of the pixel of the brain image. The local contrast (H) parameter is often used to characterize the extent of variation in pixel intensity. We adopted the stretch algorithm to compute the contrast parameter of a pixel (x_p, y_p), based on the m by m neighborhood connectivity (block B) centered at (x_p, y_p), as shown in Eq. (5), where $\min(B)$ and $\max(B)$ represented the minimum and maximum intensity values of the neighborhood pixels inside block B . The contrast parameter H was obtained by totaling the contrast of a block B , as shown in Eq. (6).

$$I_H(x_p, x_p) = \frac{I(x_p, x_p) - \max(B)}{\max(B) - \min(B)} \times \max(B) \quad (5)$$

$$H(x_p, x_p) = \sum_{(x_{p-n}, x_{p-n}) \in B} I_H(x_{p-n}, x_{p-n}) \quad (6)$$

The above three features (E, G, H) were used to compute the pixel-based similarity for the watershed segmentation.

Watershed Segmentation: Watershed segmentation is realized by considering the gray scale value of each brain pixel as the altitude of the water basin. Drops of water reach the maxima of values, and then flow along certain paths to finally reach the local minima. In this respect, the watershed corresponds to the limits of the adjacent catchment basins of the drops of water, and it also is equal to the boundary of the segmented regions. The watershed segmentation approach, a classic in image segmentation, is one of the most automated methods. The watershed segmentation technique segregates images as different intensity segments with ROIs having a high radiation density leading to high pixel intensities. Thus, the watershed segmentation is an efficient tool to classify tumors and other high intensity tissues within the brain. Watershed segmentation, as a region-based segmentation method, could also classify intensities that exhibit very small differences. Further, MWS was useful for detecting multiple regions, which could not be reached by counter-based segmentation methods such as level-set or snakes. In MWS, multiple parameters (E, G, H in Eqs. (3)–(6)) were used as different cues for watershed segmentation and led to segmented regions.

Lesion Detection: The final lesion detection was performed using ‘prior knowledge’ from ground-truth (manually derived) ROI properties, gray-scale and texture to separate lesions from other normal tissues.

2.5. Statistical comparisons

From 2D slice-based injury and brain areas ($Area_{injury}$, $Area_{brain}$), percentage lesion volumes ($V\%$) over the entire brain was determined by the equation,

$$V\% = \frac{\sum_{i=1}^{N_s} Area_{injury}(i)}{\sum_{j=1}^{N_s} Area_{brain}(j)} \quad (7)$$

where N_s equals the number of MR slices in the sequence, anterior to posterior. We further compared the performance of these computational methods, in terms of volumetric and location-overlap indices (sensitivity, specificity, and similarity) using the following equations:

$$Sensitivity = \frac{L_G \cap L_D}{L_G} \quad (8)$$

$$Specificity = \frac{(BR_G \cap L_G) \cap (BR_D \cap L_D)}{(BR_G \cap L_G)} \quad (9)$$

$$Similarity = 2 \times \frac{L_G \cap L_D}{L_G \cup L_D} \quad (10)$$

where L_G and BR_G represent the number of pixels in the ischemic injury and the entire brain, respectively, in the manually segmented data; and L_D and BR_D represent the corresponding counterparts from the detected results from each computational method.

Methods and experimental details for those reported are available upon request to the corresponding author.

3. Results

We quantitatively and qualitatively evaluated and compared all three proposed computational methods, SIRG, HRS and MWS, in their ability to identify neonatal HII lesions which were then compared to expert manual lesion extraction in clinical and rodent MRI data sets. First, we compared all three methods at a single time point when the lesion volume is static. Second, we expanded our computational assessment to test their efficacy in a temporal dataset where the lesion volume is dynamically evolving. This step is critical for clinical translation when it is often difficult to assess the time of injury, particularly in neonates. Third, our final assessment, used human neonatal data to validate that our computational methods can be readily applied in a clinically relevant manner demonstrating proof of concept.

3.1. Comparisons in an animal HII model: single time point

We compared the three methods (SIRG, HRS, MWS) using T2WI images obtained from a cohort of animals 10 days post HII induction (Fig. 4A). All three computational approaches identified virtually the same regions, with overlap to manually segmented results. However, the automated results were almost always smaller, which was confirmed in the quantitative volumetric data (Fig. 5A). SIRG performed slightly better than HRS or MWS compared to the manual segmentation (ground-truth). All three methods had close performance, based on lesion volumes (Fig. 5A) and regional sensitivity/specificity/similarity indices (Fig. 5B) both for entire 3D volume and individual 2D MR slices from anterior to posterior brain imaging sections.

3.2. Comparisons in an animal HII model: temporal lesion evolution

We further extended our computational analysis of the three methods (SIRG, HRS, MWS) to determine their ability to identify HII lesions as they evolve over time. We utilized T2WI data that spanned between 1–31 days post HII and performed volumetric

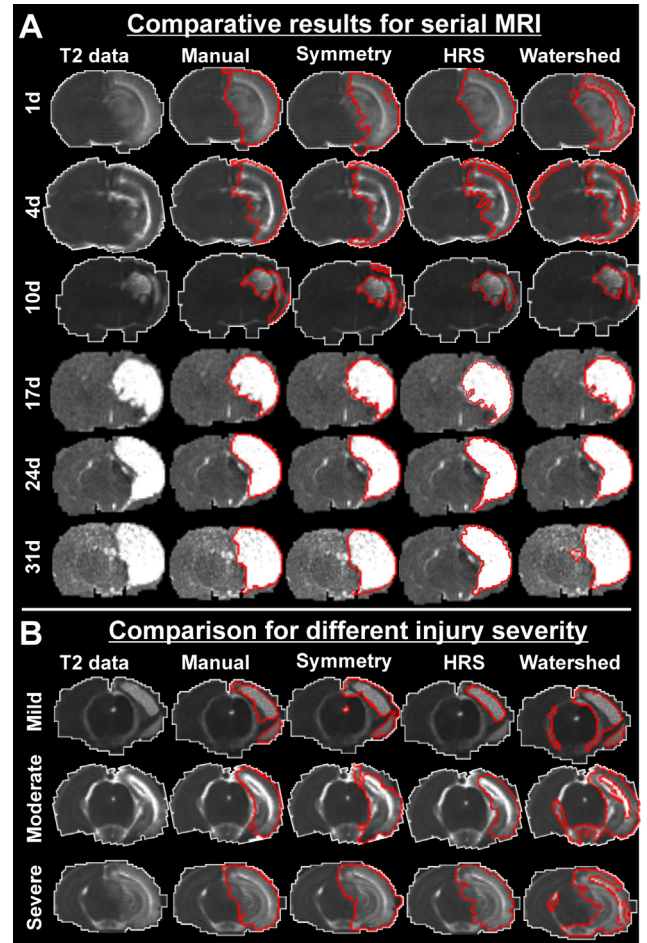


Fig. 4. Comparative results for (A) temporal MRI and for (B) graded injury severities in a rat-pup model of ischemia. (A) Detection by all three methods largely overlapped with the manual detection over the temporal data and were often better at later time points (17–31 days). For the earlier time-points (1–10 days), MWS method resulted in some misclassifications, while SIRG and HRS produced more accurate and similar results (Table 5 summarizes the performance of different methods in terms of overlap in injury locations for entire 3D volumes, as well as for individual 2D slices). (B) For different injury severities all three methods resulted in comparable results. SIRG performed well for all severity types, with few false positive (mild) or false negative (moderate) detections. HRS under-estimated mild and moderate injuries but performed the best (among the three methods compared) for severe injury. MWS method was more prone to detect outliers at all injury severities compared to other two methods. (Respective overlap measures are summarized in Table 6.)

(Fig. 5C) and performance comparisons (Table 5) for both the entire 3D volumes and the individual 2D slices. The ischemic injury initially decreased with time and then increased towards its final volume (Fig. 5C). Volumetrically, SIRG and HRS performed the best at 3 time-points each (SIRG: 4 days, 17 days, 31 days; HRS: 1 day, 7 days, 24 days post HII), while MWS results varied most widely and performed best only at 1 time-point (10 days post HII). Performance comparisons for the entire 3D volume (Table 5) indicated SIRG performed the best (13/21 cases) compared to HRS (6/21 cases) and MWS (2/21 cases). When evaluated for performance in individual 2D MR slices, anterior to posterior brain, HRS had the lowest standard deviations (in 62% cases) and hence was the most robust compared to SIRG (29% cases) and MWS (9% cases) (Table 5).

3.3. Comparisons in an animal HII model: discrimination of injury severity

To compare the performance of SIRG, HRS and MWS in injury severity discrimination, we further classified injury based on

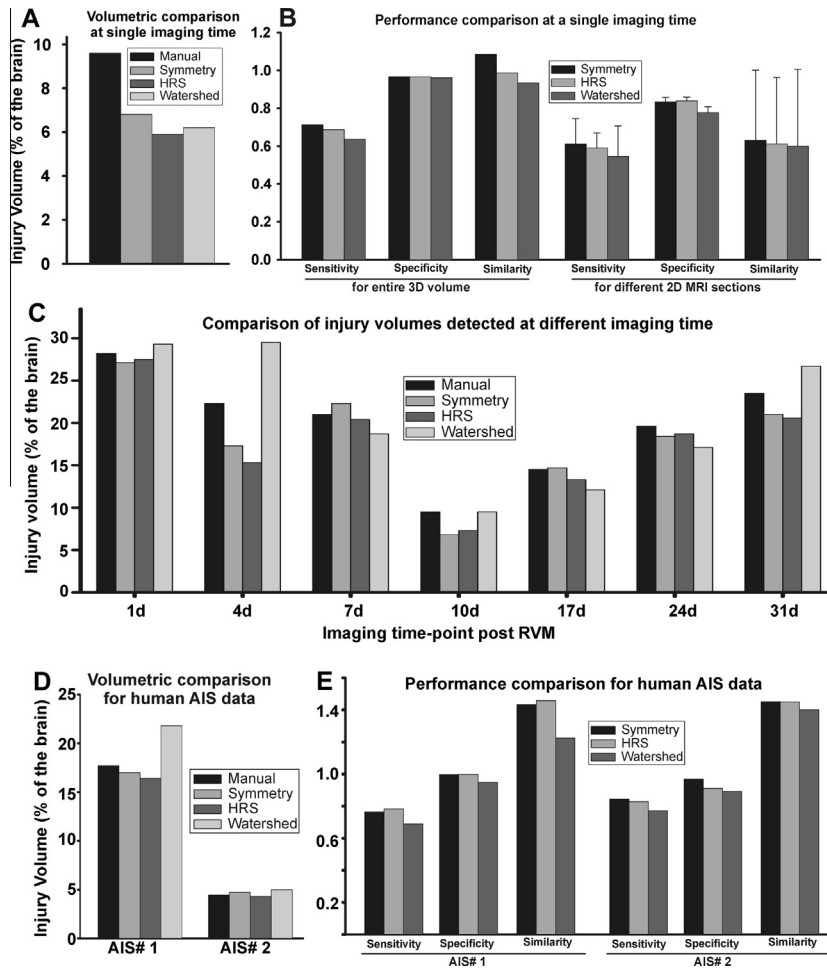


Fig. 5. Summary of performance indices. For neonatal rats, lesion volumes between the three methods (SIRG, HRS, MWS) compared for 3D volumes (A) and in performance over 2D MRI slices (B). Volumetric comparisons for temporal data (1–31 days post ischemia) in HII rat pups (C) illustrates that all three methods followed manual detections at most of the imaging time-points. At 4d when SIRG and HRS underestimated and MWS overestimated with respect to manual detection. Regional overlap comparisons are also summarized in Table 5 for entire 3D volume as well as for variations across different MRI sections. The temporal variation of HII severity is shown in C. Volumetric comparisons (D) and 3D regional overlaps (E) are summarized for two AIS patients (severe, mild) with respect to respective manual detections.

manually detected lesion volumes as mild (<10%), moderate (10–25%) or severe (>25%) injury (Fig. 4B). Volumetrically, SIRG performed the best for mild and moderate injury, while HRS was best for severe injury (Fig. 4B). Similar performance trends were observed for sensitivity, specificity and similarity (Table 6). MWS had lower performance than SIRG and HRS in both these respects.

3.4. Neonatal AIS: single time point

Finally, we evaluated SIRG, HRS, and MWS methods in neonatal AIS patients with a range of injury severities, specifically using ADC maps computed from DWI data. All three methods successfully extracted the AIS lesion (Fig. 3B) that was found in two regionally distinct brain areas. Scalar volumetric comparison (Fig. 5D) and performance indices (Fig. 5E) revealed that HRS and SIRG had comparable performance, while MWS lagged behind in both respects, suffering from over-estimation (false positives), particularly when the injury was more severe.

A close inspection of regional overlap indices (Fig. 5E) revealed that for a larger AIS lesion (17.7% of total brain volume, Fig. 3B, Fig. 5D) HRS outperformed SIRG (Fig. 5E, AIS#1), while for a smaller AIS lesion (4.5% of total brain volume, Fig. 5D) SIRG outperformed HRS (Fig. 5E, AIS#2).

4. Discussion

In experimental and clinical ischemic injury, lesion locations are often abnormal foci within normal brain tissues that vary in location, size and shape, and are likely comprised of different MR characteristics (i.e., T2 relaxation times, ADC values or their associated image intensities). Automated detection of HII lesions from MRI could potentially help in candidate selection, treatment and monitoring (Ghosh et al., 2012a; Wechsler, 2011), specifically for neonatal HII where current prior-model based alignment techniques (Table 2) fail due to developmental changes within maturing brains.

We compared three state-of-the-art region-based injury detection methods – symmetry integrated region growing (SIRG) (Sun et al., 2009), hierarchical region splitting (HRS) (Ghosh et al., 2011), and modified watershed segmentation (MWS) (Ratan et al., 2009) – none of which require model-subject alignment or co-registration. All three methods automatically detected lesion volume from either T2-relaxation or ADC maps of clinical AIS neonates and experimental animals with HII. Their volumetric and location-overlap performance were computed with respect to the manually detected ground-truth data and compared for accuracy and robustness. With respect to different MRI acquisitions, in the clinic, diffusion weighted imaging (DWI) is used predominately

Table 5

Comparison of temporal performance measures following experimental HII. Computations were assessed over the entire 3D MRI volume or over individual 2D MRI slice volumes. Shaded and bolded entries are optimal for their respective comparisons.

Overlap measures	Time post injury	Based on entire 3D MRI volume			Based on individual 2D MRI slices		
		SIRG	HRS	MWS	SIRG	HRS	MWS
Sensitivity	1 day	0.81	0.81	0.77	0.62 ± 0.26	0.69 ± 0.26	0.66 ± 0.22
	4 days	0.87	0.81	0.68	0.66 ± 0.19	0.62 ± 0.14	0.61 ± 0.29
	7 days	0.88	0.88	0.70	0.75 ± 0.23	0.72 ± 0.19	0.52 ± 0.24
	10 days	0.71	0.69	0.63	0.71 ± 0.16	0.69 ± 0.09	0.64 ± 0.19
	17 days	0.90	0.87	0.81	0.71 ± 0.16	0.71 ± 0.11	0.68 ± 0.22
	24 days	0.88	0.77	0.85	0.69 ± 0.26	0.61 ± 0.28	0.59 ± 0.36
	31 days	0.84	0.85	0.82	0.64 ± 0.21	0.67 ± 0.24	0.63 ± 0.21
Specificity	1 day	0.94	0.92	0.89	0.95 ± 0.05	0.95 ± 0.03	0.94 ± 0.04
	4 days	0.91	0.92	0.85	0.92 ± 0.06	0.93 ± 0.05	0.91 ± 0.05
	7 days	0.97	0.95	0.97	0.93 ± 0.02	0.93 ± 0.07	0.93 ± 0.04
	10 days	0.97	0.97	0.96	0.97 ± 0.03	0.98 ± 0.02	0.91 ± 0.04
	17 days	0.98	0.96	1.00	0.98 ± 0.02	0.96 ± 0.02	0.99 ± 0.04
	24 days	0.99	0.92	0.97	0.98 ± 0.01	0.91 ± 0.02	0.97 ± 0.03
	31 days	0.98	0.96	0.98	0.98 ± 0.03	0.95 ± 0.02	0.98 ± 0.04
Similarity	1 day	1.40	1.41	1.21	1.08 ± 0.40	1.12 ± 0.38	0.97 ± 0.43
	4 days	1.23	1.18	0.79	0.96 ± 0.38	0.94 ± 0.39	0.70 ± 0.39
	7 days	1.34	1.31	0.98	0.98 ± 0.35	0.94 ± 0.30	0.64 ± 0.38
	10 days	1.09	0.99	0.93	0.73 ± 0.43	0.71 ± 0.41	0.70 ± 0.47
	17 days	1.62	1.44	1.68	0.92 ± 0.43	0.86 ± 0.49	0.89 ± 0.50
	24 days	1.67	1.67	1.62	0.90 ± 0.35	0.91 ± 0.32	0.89 ± 0.34
	31 days	1.59	1.59	1.55	0.88 ± 0.39	0.88 ± 0.34	0.86 ± 0.34

Table 6

Comparison of performance measures for mild, moderate and severe injury for the three methods. Computations were performed over the entire 3D MRI volumes. Shaded and bolded entries are the optimal indices for their respective comparisons.

Measures	Severity	SIRG	HRS	MWS
Sensitivity	Mild	0.71	0.69	0.63
	Moderate	0.87	0.81	0.68
	Severe	0.81	0.81	0.77
Specificity	Mild	0.97	0.97	0.96
	Moderate	0.91	0.92	0.85
	Severe	0.94	0.92	0.89
Similarity	Mild	1.09	0.99	0.93
	Moderate	1.23	1.18	0.79
	Severe	1.40	1.41	1.21

to monitor early ischemic injury, so we undertook assessment of our algorithms using clinically relevant imaging sequences/data. SIRG and HRS performed equally well on T2- or diffusion weighted imaging. Thus, one could suggest that either SIRG/HRS can be used on a variety of clinically relevant imaging sequences. The key results were: (1) SIRG performed best for lesion volumes and location for the entire 3D MRI data set; (2) HRS was most robust (with lowest standard deviation) over individual 2D MR slices; and (3) MWS was out-performed by SIRG and HRS in all respects.

Current MRI based lesion extraction techniques (Table 1) mostly adopt one of the two following approaches. (A) Healthy tissue segmentation followed by abnormality (lesion) extraction. Here prior models are used to classify healthy tissues into different anatomical regions (Birgani et al., 2008; Kabir et al., 2007) or a single normal tissue class (Cuadra et al., 2004; Van Leemput et al., 2001) and then the outlier regions that do not satisfy any normal tissue class are designated as lesion. A significant weakness of this approach is the requirement for a large volume of training data (to fit all normal tissue or complex prior models for anatomy) which is often not readily available, particularly for neonates. (B) Digital subtraction to detect changes in longitudinal (serial) MR data (Manana et al., 2006; Sadasivan et al., 2009). However, accurate subtraction requires temporal datasets, and 2D or 3D registration among serial MRI data which often suffers when neuroimaging time-points are too far apart for rapidly maturing

neonatal brains (Klein et al., 2010; Zhiguo et al., 2005; Zitova; and Flusser, 2003).

Curve fitting of tissue-boundaries based on partial differential equations, including parametric methods like active contour snakes (Kazerooni et al., 2011; Liang et al., 2006; Zhou and Xie, 2013), non-parametric methods like level-set propagation (Droske et al., 2001), and their several modified versions (Bai et al., 2013; Kazemifar et al., 2014; Le Guyader and Vese, 2008; Liang et al., 2006; Mesejo et al., 2014; Somkantha et al., 2011; Wang et al., 2013) have been adopted in different medical image analysis applications. Success of these methods heavily depends on MRI intensity contrast edge detection (Kazerooni et al., 2011; Liang et al., 2006; Somkantha et al., 2011), seed-initialization (which is often manual) (Zhou and Xie, 2013) and choice of energy function (Kazerooni et al., 2011; Liang et al., 2006) that is to be minimized by heuristic gradient descent algorithms (Wang et al., 2013). These methods are often computationally expensive due to the need for an initial training module (Kazemifar et al., 2014; Mesejo et al., 2014), need for manual interventions (Liang et al., 2006; Zhou and Xie, 2013), need for obtaining global-minima during energy minimization instead of local-minima (inherent problem of greedy search in gradient descent algorithms) (Mesejo et al., 2014; Wang et al., 2013) and sometime requires prior models (Bai et al., 2013; Le Guyader and Vese, 2008; Wang et al., 2013) or atlas-registration (Kazemifar et al., 2014) with their associated limitations as mentioned earlier. These pitfalls often restrict use of level-set and active contour snake methods in real-time clinical applications. SIRG, HRS and MWS methods compared in this paper do not utilize atlas or prior models, reduce computational complexity to a large extent, and perform segmentation without manual intervention.

Further, MRI data issues are aggravated by ROI fuzziness (Table 2). Motion artifacts and noise levels (Table 2, problem ID 3) might be partially reduced with conventional image filtering in some cases (Klein et al., 2010; Zhiguo et al., 2005; Zitova; and Flusser, 2003). ROI contrast and sharpness enhancement (Table 2, problem ID 1 and 2) based on low-level image features fails unless complex prior models are utilized (Birgani et al., 2008; Cuadra et al., 2004; Kabir et al., 2007; Manana et al., 2006; Van Leemput et al., 2001; Zhiguo et al., 2005). Model-subject registration

(Cuadra et al., 2004; Schmidt et al., 2005) also suffers when injury crosses anatomical boundaries (Ghosh et al., 2012a) and/or when noisy low-level features, including image intensity (Kabir et al., 2007), texture (Krugger et al., 2008), shape, and 3D volume (Liu et al., 2005), are used to align multiple data and time points.

In summary, the majority of current ROI extraction methods depend heavily on large amounts of training data (often not available), significant preprocessing (time-consuming), complex prior models (often not reliable, specifically for neonates), model-subject registration (labor-intensive) and significant user intervention (human bias) that reduce their practical applicability in real-time medical image analysis (Neumann-Haefelin and Steinmetz, 2007). The three methods compared in this paper – SIRG, HRS and MWS – do not require model-subject alignment nor any training data, and very little prior knowledge for injury classification in HRS and MWS (Tables 1 and 2). They effectively handle ROI detection problems using only high-level features like symmetry and mean MR or grayscale values representative of the injury (Table 2). This also significantly reduces computational complexity, required for practical real-time clinical applications.

When the three methods were compared, they all performed satisfactorily, correlating with the manual ground-truth for clinical AIS (Fig. 3B) and in an animal model of HII, for temporal evolution (Fig. 4A) and for different injury severities (Fig. 4B). SIRG performed the best for scalar percent-volumes (Fig. 5A) and regional overlaps (Fig. 5B). Interestingly, substantial performance variations (mean \pm standard deviation) were observed over different MR slices anterior to posterior portion of the brain when SIRG was used (Fig. 5B). Lower variations indicate more robustness and stability of the methods, and this is where we observed that HRS performed the best. In our manual “ground truth” data, there were some cases where an experienced researcher manually included regions (e.g., lateral portions of the ventral cortex in Fig. 4A, 10 days) that were not identified by any of the computational approaches. This was reflected in volumetric comparisons (Fig. 5A) and in larger variations in similarity (Fig. 5B), which effectively measures regional precision for detection (ratio of true positive over false negative).

HII lesions are very dynamic as the brain responds to the injury (Ashwal et al., 2007; Obenaus et al., 2011a). Volumetric temporal evolution of HII matched well with previously published results (Obenaus et al., 2011b). Again SIRG and HRS had close 3D volumetric performance (Fig. 5C) while HRS was the most robust (Table 5) with serial MRI assessments. Similarly, variation in injury severity in clinical and animal HII and could be correctly distinguished by all three methods (Fig. 4B, Fig. 5D) (Ghosh et al., 2012b). Interestingly, SIRG performance was best in mild and moderate HII while HRS was better for severe HII (Table 5). Previous studies have noted that a limitation of HRS is that it does not perform well in mild injuries (Ghosh et al., 2011), which we confirmed here. Similar trends were also observed in clinical AIS where HRS results overlapped best for larger injuries whereas SIRG had better results for small injuries (Fig. 5E).

The SIRG approach (Sun et al., 2009) utilized symmetry as a high level feature and 3D connectivity based outlier rejection that significantly improved its power for injury discrimination, despite noisy, blurred or motion-affected boundaries seen in MRI. A limitation of SIRG lies in extensive tuning of many parameters (compared to HRS and MWS; Table 2) which may be even injury-specific. SIRG would also fail in challenging cases where brain structure lacks defined symmetry or the injury itself is symmetric (bilateral) with regard to the axis of the brain (Ghosh et al., 2011). Fusion of SIRG with HRS and using prior MR knowledge, particularly using quantitative T2/ADC values could potentially solve this weakness. The strength of HRS (Ghosh et al., 2011) lies in the use of a small set of parameters (Table 2), stable bipartite segmentation

leading to robustness (lowest variations; Table 5) as well as using quantitative MR values (T2 relaxation times, ADC) that assist in improved HII lesion detection from healthy tissue. Limitations of HRS were that, (a) it did not consider 3D connectivity of injury for inclusion and exclusion of sub-regions and (b) it underperformed for mild injury because of small ROIs. Fusing symmetry features and 3D asymmetric volume models (Fig. 1) from SIRG may mitigate these HRS weaknesses. The MWS approach (Ratan et al., 2009) was always the least effective method evaluated in this paper (Fig. 5, Tables 5 and 6). MWS suffered from over-segmentation inherent in watershed methods (Ratan et al., 2009), insufficient cues to reject outliers, and used additional noisy non-injury regions as prior information (Fig. 5A). This resulted in many false positives in MWS detected injury (Fig. 4B) that significantly reduced its performance (Fig. 5, Table 6). Symmetry cues and use of quantitative MR values might improve MWS results (Fig. 4B).

A short note on how much time is required to run these algorithms. We have used the term “real-time” to further demonstrate that both SIRG and HRS could be used clinically in the context of rapid stroke or ischemic patient treatment. Although SIRG and MWS take couple of hours for training the respective parameters, once trained they can identify lesion or injured tissues from MRI data in less than 5 minutes. Further, HRS does not require any training and once the data are skull-stripped it can produce lesion results within 15 s. Hence, these algorithms could be used by clinical neurologists in treatment paradigms where early intervention is often desirable.

5. Conclusions

In conclusion, unlike most of the current methods, the three region-based injury detection methods assessed – SIRG, HRS and MWS – are objective and robust for real-time clinical applications. They do not require labor-intensive preprocessing, complex prior-models and model-subject alignment. Specifically for neonatal ischemic injury, SIRG performed best overall but HRS was the most robust, and fusion of these two techniques in future studies has a greater potential for automated injury detection from brain MRI data.

Acknowledgements

This study was supported by funding in part by National Science Foundation Integrative Graduate Education and Research Traineeship (IGERT) in Video Bioinformatics (DGE 0903667 to BB). The authors wish to acknowledge the Department of Radiology at LLU Medical Center for assistance with the clinical data. This research was further supported by funds from the Department of Pediatrics, Loma Linda University; and NIH NINDS (1R01NS059770 to SA).

References

- Ahbeek, P., Vincken, K.L., Groenendaal, F., Koeman, A., van Osch, M.J., van der Grond, J., 2008. Probabilistic brain tissue segmentation in neonatal magnetic resonance imaging. *Pediatr. Res.* 63, 158–163.
- Ashwal, S., Tone, B., Tian, H.R., Chong, S., Obenaus, A., 2007. Comparison of two neonatal ischemic injury models using magnetic resonance imaging. *Pediatr. Res.* 61, 9–14.
- Bai, P.R., Liu, Q.Y., Li, L., Teng, S.H., Li, J., Cao, M.Y., 2013. A novel region-based level set method initialized with mean shift clustering for automated medical image segmentation. *Comput. Biol. Med.* 43, 1827–1832.
- Bergo, F.P.G., Falcao, A.X., Yasuda, C.L., Cendes, F., 2008. FCD segmentation using texture asymmetry of MR-T1 images of the brain. In: *Proc. IEEE Intl. Symp. Biomedical Imaging (ISBI)*, pp. 424–427.
- Bhanu, B., Parvin, B.A., 1987. Segmentation of natural scenes. *Pattern Recogn.* 20, 487–496.

- Bilmes, J.A., 1998. A Gentle Tutorial of the EM Algorithm and its Application to Parameter Estimation for Gaussian Mixed and Hidden Markov Models. UC Berkeley, pp. April TR-97-02.
- Birgani, P.M., Ashtiyani, M., Asadi, S., 2008. MRI segmentation using fuzzy C-means clustering algorithm basis neural network. In: Proc. IEEE Intl. Conf. on Information & Communication Tech., pp. 1–5.
- Corso, J.J., Sharon, E., Dube, S., El-Saden, S., Sinha, U., Yuille, A., 2008. Efficient multilevel brain tumor segmentation with integrated Bayesian model classification. *IEEE Trans. Med. Imag.* 27, 629–640.
- Cuadra, M.B., Pollo, C., Bardera, A., Cuisenaire, O., Villemure, J.G., Thiran, J.P., 2004. Atlas-based segmentation of pathological MR brain images using a model of lesion growth. *IEEE Trans. Med. Imag.* 23, 1301–1314.
- Droske, M., Meyer, B., Rumpf, M., Schaller, C., 2001. An adaptive level set method for medical image segmentation. In: Proceedings of the 17th Int. Conf. of Information Processing in Medical Imaging (IPMI) Springer-Verlag Davis, CA, USA, pp. 416–422.
- Du, Q., Kopriva, I., 2008. Automated target detection and discrimination using constrained kurtosis maximization. *IEEE Geosci. Remote Sens. Lett.* 5, 38–42.
- Ghosh, N., Recker, R., Shah, A., Bhanu, B., Ashwal, S., Obenaus, A., 2011. Automated ischemic lesion detection in a neonatal model of hypoxic ischemic injury. *J. Magn. Reson. Imag.* 33, 772–781.
- Ghosh, N., Sun, Y., Turenius, C., Bhanu, B., Obenaus, A., Ashwal, S., 2012a. *Comput. Anal.: Brid. Trans. Stroke Treat.. Translational Stroke Research.* Springer New York, New York, NY, pp. 881–909.
- Ghosh, N., Yuan, X., Turenius, C., Tone, B., Ambadipudi, K., Snyder, E.Y., Obenaus, A., Ashwal, S., 2012b. Automated core-penumbra quantification in neonatal ischemic brain injury. *J. Cereb. Blood Flow Metab.* 32, 2161–2170.
- Gupta, A., Prasad, V.S.N., Davis, L.S., 2005. Extracting regions of symmetry. In: Proc. IEEE Intl. Conf. Image Processing (ICIP), vol. 3, pp. 133–136.
- Hojjatolleslami, S.A., Kruggel, F., 2001. Segmentation of large brain lesions. *IEEE Trans. Med. Imag.* 20, 666–669.
- Kabir, Y., Dojat, M., Scherrer, B., Forbes, F., Garbay, C., 2007. Multimodal MRI segmentation of ischemic stroke lesions. In: Conference Proceedings: Annual International Conference of the IEEE Engineering in Medicine and Biology Society. IEEE Engineering in Medicine and Biology Society, Conference 2007, pp. 1595–1598.
- Kazemifard, S., Drozd, J.J., Rajakumar, N., Borrie, M.J., Bartha, R., Alzheimer's Disease Neuroimaging, I., 2014. Automated algorithm to measure changes in medial temporal lobe volume in Alzheimer disease. *J. Neurosci. Methods.*
- Kazerouni, A.F., Ahmadian, A., Serej, N.D., Rad, H.S., Saberi, H., Yousefi, H., Farnia, P., 2011. Segmentation of brain tumors in MRI images using multi-scale gradient vector flow. In: Conference Proceedings: Annual International Conference of the IEEE Engineering in Medicine and Biology Society. IEEE Engineering in Medicine and Biology Society, Conference 2011, pp. 7973–7976.
- Kharrat, A., Benamrane, N., Messaoud, M.B., Abid, M., 2009. Detection of brain tumor in medical images. In: Proc. IEEE Intl. Conf. Signals, Circuits and Systems (ICSCS), pp. 1–6.
- Khotanlou, H., Colliot, O., Atif, J., Bloch, I., 2009. 3D Brain tumor segmentation in MRI using fuzzy classification, symmetry analysis and spatially constrained deformable models. *Fuzzy Sets Syst.* 160, 1457–1473.
- Klein, S., Staring, M., Murphy, K., Viergever, M.A., Pluim, J.P., 2010. Elastix: a toolbox for intensity-based medical image registration. *IEEE Trans. Med. Imag.* 29, 196–205.
- Kruggel, F., Paul, J.S., Gertz, H.J., 2008. Texture-based segmentation of diffuse lesions of the brain's white matter. *Neuroimage* 39, 987–996.
- Le Guyader, C., Vese, L.A., 2008. Self-repelling snakes for topology-preserving segmentation models. *IEEE Trans. Image Process.: Publ. IEEE Signal Process. Soc.* 17, 767–779.
- Liang, J., McInerney, T., Terzopoulos, D., 2006. United snakes. *Med. Image Anal.* 10, 215–233.
- Liu, J., Udupa, J.K., Odhner, D., Hackney, D., Moonis, G., 2005. A system for brain tumor volume estimation via MR imaging and fuzzy connectedness. *Comput. Med. Imag. Graph.: Off. J. Comput. Med. Imag. Soc.* 29, 21–34.
- Lowe, D.G., 2004. Distinctive image features from scale-invariant keypoints. *Int. J. Comput. Vision* 60, 91–110.
- Manana, G., Romero, E., Gonzalez, F., 2006. A grid computing approach to subtraction radiography. In: Proc. IEEE Intl. Conf. Image Processing (ICIP), pp. 3325–3328.
- Mesejo, P., Valsecchi, A., Marrakchi-Kacem, L., Cagnoni, S., Damas, S., 2014. Biomedical image segmentation using geometric deformable models and metaheuristics. *Comput. Med. Imag. Graph.: Off. J. Comput. Med. Imag. Soc.*
- Nan, Z., Ruan, S., Lebonvallet, S., Qingmin, L., Yuemin, Z., 2009. Multi-kernel SVM based classification for brain tumor segmentation of MRI multi-sequence. In: Proc. IEEE Intl. Conf. Image Processing (ICIP), pp. 3373–3376.
- Neumann-Haefelin, T., Steinmetz, H., 2007. Time is brain: is MRI the clock? *Curr. Opin. Neurol.* 20, 410–416.
- Niimi, T., Imai, K., Maeda, H., Ikeda, M., 2007. Information loss in visual assessments of medical images. *Eur. J. Radiol.* 61, 362–366.
- Obenaus, A., Dilmac, N., Tone, B., Tian, H.R., Hartman, R., Digicaylioglu, M., Snyder, E.Y., Ashwal, S., 2011a. Long-term magnetic resonance imaging of stem cells in neonatal ischemic injury. *Ann. Neurol.* 69, 282–291.
- Obenaus, A., Dilmac, N., Tone, B., Tian, H.R., Hartman, R., Digicaylioglu, M., Snyder, E.Y., Ashwal, S., 2011b. Long-term magnetic resonance imaging of stem cells in neonatal ischemic injury. *Ann. Neurol.* 69, 1531–8249.
- Otsu, N., 1979. A threshold selection method from gray-level histograms. *IEEE Trans. Syst. Man Cybern.* 9, 62–66.
- Prasad, V.S., Yegnanarayana, B., 2004. Finding axes of symmetry from potential fields. *IEEE Trans. Image Process.: Publ. IEEE Signal Process. Soc.* 13, 1559–1566.
- Ratan, R., Sharma, S., Sharma, S.K., 2009. Brain tumor detection based on multi-parameter MRI image analysis. *Int. Congr. Global Sci. Technol. (ICGST) Int. J. Graph. Vision Image Process. (GVIP)* 9, 9–17.
- Ray, N., Saha, B.N., Brown, M.R.G., 2007. Locating brain tumors from MR imagery using symmetry. In: Proc. IEEE Asilomar Conf. Signals, Systems, and Computers (ACSSC), pp. 224–228.
- Sadasivan, C., Cesar, L., Seong, J., Wakhloo, A.K., Lieber, B.B., 2009. Treatment of rabbit elastase-induced aneurysm models by flow diverters: development of quantifiable indexes of device performance using digital subtraction angiography. *IEEE Trans. Med. Imag.* 28, 1117–1125.
- Saha, S., Bandyopadhyay, S., 2007. MRI brain image segmentation by fuzzy symmetry based genetic clustering technique. *Proc. IEEE Congr. Evol. Comput.*, 4417–4424.
- Schiemanck, S.K., Kwakkkel, G., Post, M.W., Prevo, A.J., 2006. Predictive value of ischemic lesion volume assessed with magnetic resonance imaging for neurological deficits and functional outcome poststroke: a critical review of the literature. *Neurorehab. Neural Re.* 20, 492–502.
- Schmidt, M., Levner, I., Greiner, R., Murtha, A., Bistritz, A., 2005. Segmenting brain tumors using alignment-based features. In: Proc. IEEE Intl. Conf. Machine Learning and Applications (ICMLA), pp. 215–220.
- Somkantha, K., Theera-Umporn, N., Auephanwiriyakul, S., 2011. Boundary detection in medical images using edge following algorithm based on intensity gradient and texture gradient features. *IEEE Trans. Bio-Med. Eng.* 58, 567–573.
- Sun, Y., Bhanu, B., 2009. Symmetry integrated region-based image segmentation. In: Proc. IEEE Intl. Conf. Computer Vision and Pattern Recognition (CVPR), pp. 826–831.
- Sun, Y., Bhanu, B., Bhanu, S., 2009. Automatic symmetry-integrated brain injury detection in MRI sequences. In: IEEE Computer Society Workshop on Mathematical Methods in Biomedical Image Analysis. Held in Conjunction with IEEE Computer Society Conference on Computer Vision and Pattern Recognition, June 20–25, 2009. IEEE, Miami Beach, FL, pp. 79–86.
- Sun, Y., Bhanu, B., 2012. Reflection symmetry integrated image segmentation. *IEEE Trans. Pattern Anal. Mach. Intell.* 34, 1827–1841.
- Van Leemput, K., Maes, F., Vandermeulen, D., Colchester, A., Suetens, P., 2001. Automated segmentation of multiple sclerosis lesions by model outlier detection. *IEEE Trans. Med. Imag.* 20, 677–688.
- Wang, L., Yu, Z., Pan, C., 2013. A unified level set framework utilizing parameter priors for medical image segmentation. *Sci. China Inf. Sci.* 56, 1–14.
- Wechsler, L.R., 2011. Imaging evaluation of acute ischemic stroke. *Stroke* 42, pp. S12–S15.
- Zhiguo, C., Xiaoxiao, L., Bo, P., Yiu-Sang, M., 2005. DSA image registration based on multiscale gabor filters and mutual information. In: Proc. IEEE Intl. Conf. Information Acquisition, pp. 105–110.
- Zhou, W., Xie, Y., 2013. Interactive medical image segmentation using snake and multiscale curve editing. *Comput. Math. Methods Med.* 2013, 325903.
- Zitovaj, B., Flusser, J., 2003. Image registration methods: a survey. *Image Vision Comput.* 21, 977–1000.